Side-illumination fluorescence critical angle: theory and application to F8BT-doped polymer optical fibers

Iñaki Bikandi,* **María Asunción Illarramendi, Joseba Zubia, Jon Arrue, and Felipe Jiménez**

University of the Basque Country, ETSI de Bilbao, Alda. Urquijo s/n, E-48013 Bilbao, Spain
**inaki.bikandi@ehu.es*

Abstract: In this work we have analyzed theoretically and experimentally the critical angle for the emission generated in doped polymer optical fibers as a function of different launching conditions by using the side-illumination fluorescence technique. A theoretical model has been developed in order to explain the experimental measurements. It is shown that both the theoretical and experimental critical angles are appreciably higher than the meridional critical angle corresponding to the maximum acceptance angle for a single source placed at the fiber axis. This increase changes the value of several important parameters in the performance of active fibers. The analysis has been performed in polymer optical fibers doped with a conjugated polymer.

OCIS codes: (060.2300) Fiber measurements; (060.2310) Fiber optics; (060.2400) Fiber properties; (300.2140) Emission.

References and links

1. J. Zubia and J. Arrue, “Plastic optical fibers: an introduction to their technological processes and applications,” Opt. Fiber Technol. **7**(2), 101–140 (2001).
2. T. Kaino, “Polymer optical fibers,” in *Polymers for Lightwave and Integrated Optics* (Marcel Dekker, Inc., 1992), chap. 1.
3. O. Ziemann, J. Krauser, P. E. Zamzow, and W. Daum, *POF Handbook: Optical Short Range Transmission Systems,* 2nd ed. (Springer, 2008).
4. D. Kalymnios, P. Scully, J. Zubia, and H. Poisel, “POF sensors overview,” in *Proceedings of the 13th international plastic optical fibers conference*, (Nürnberg, 2004), pp. 237–244.
5. H. Liang, Z. Zheng, Z. Li, J. Xu, B. Chen, H. Zhao, Q. Zhang, and H. Ming, “Fabrication and amplification of rhodamine B-doped step-index polymer optical fiber,” J. Appl. Polym. Sci. **93**(2), 681–685 (2004).
6. A. Tagaya, S. Teramoto, E. Nihei, K. Sasaki, and Y. Koike, “High-power and high-gain organic dye-doped polymer optical fiber amplifiers: novel techniques for preparation and spectral investigation,” Appl. Opt. **36**(3), 572–578 (1997).
7. J. Clark and G. Lanzani, “Organic photonics for communications,” Nat. Photonics **4**(7), 438–446 (2010).
8. C. Pulido and O. Esteban, “Improved fluorescence signal with tapered polymer optical fibers under side-illumination,” Sens. Actuators B Chem. **146**(1), 190–194 (2010).
9. C. Pulido and O. Esteban, “Multiple fluorescence sensing with side-pumped tapered polymer fiber,” Sens. Actuators B Chem. **157**(2), 560–564 (2011).
10. H. Y. Tam, C.-F. Jeff-Pun, G. Zhou, X. Cheng, and M. L. V. Tse, “Special structured polymer fibers for sensing applications,” Opt. Fiber Technol. **16**(6), 357–366 (2010).
11. M. Sheeba, K. J. Thomas, M. Rajesh, V. P. N. Nampoori, C. P. G. Vallabhan, and P. Radhakrishnan, “Multimode laser emission from dye doped polymer optical fiber,” Appl. Opt. **46**(33), 8089–8094 (2007).
12. G. V. Maier, T. N. Kopylova, V. A. Svetlichnyi, V. M. Podgaetskii, S. M. Dolotov, O. V. Ponomareva, A. E. Monich, and E. A. Monich, “Active polymer fibers doped with organic dyes: generation and amplification of coherent radiation,” Quantum Electron. **37**(1), 53–59 (2007).
13. J. Clark, L. Bazzana, D. Bradley, J. Gonzalez, G. Lanzani, D. Lidzey, J. Morgado, A. Nocivelli, W. Tsoi, T. Virgili, and R. Xia, “Blue polymer optical fiber amplifiers based on conjugated fluorine oligomers,” J. Nanophoton. **2**(1), 023504 (2008).

#159505 - $15.00 USD Received 5 Dec 2011; revised 23 Jan 2012; accepted 23 Jan 2012; published 9 Feb 2012

14. M. A. Illarramendi, J. Zubia, L. Bazzana, G. Durana, G. Aldabaldetreku, and J. R. Sarasua, "Spectroscopic characterization of plastic optical fibers doped with fluorene oligomers," J. Lightwave Technol. **27**(15), 3220–3226 (2009).
15. R. J. Potter, "Transmission properties of optical fibers," J. Opt. Soc. Am. **51**(10), 1079–1089 (1961).
16. Y. Xu, A. Cotteden, and N. B. Jones, "A theoretical evaluation of fibre-optic evanescent wave absorption in spectroscopy and sensors," Opt. Lasers Eng. **44**(2), 93–101 (2006).
17. A. W. Snyder and J. D. Love, *Optical waveguide theory* (Chapman and Hall, 1983).
18. W. L. Barnes, S. B. Poole, J. E. Townsend, L. Reekie, D. J. Taylor, and D. N. Payne, "Er3+ -Yb3+ and Er3+ doped fiber lasers," J. Lightwave Technol. **7**(10), 1461–1465 (1989).
19. C. P. Achenbach and J. H. Cobb, "Computational studies of light acceptance and propagation in straight and curved multimodal active fibres," J. Opt. A, Pure Appl. Opt. **5**(3), 239–249 (2003).
20. I. Ayesta, J. Arrue, F. Jimenez, M. A. Illarramendi, and J. Zubia, "Computational analysis of the amplification features of active plastic optical fibers," Phys. Status Solidi A **208**(8), 1845–1848 (2011).
21. J. Arrue, F. Jimenez, I. Ayesta, M. A. Illarramendi, and J. Zubia, "Polymer-optical-fiber lasers and amplifiers doped with organic dyes," Polymers **3**(3), 1162–1180 (2011).
22. Y. Zhao and S. Fleming, "Analysis of the effect of numerical aperture on Pr:ZBLAN upconversion fiber lasers," Opt. Lett. **23**(5), 373–375 (1998).
23. M. J. Adams, *An introduction to optical waveguides* (John Wiley & Sons, 1981).
24. R. J. Kruhlak and M. G. Kuzyk, "Side-illumination fluorescence spectroscopy. I. Principles," J. Opt. Soc. Am. B **16**(10), 1749–1755 (1999).
25. R. J. Kruhlak and M. G. Kuzyk, "Side-illumination fluorescence spectroscopy. II. applications to squaraine-dye-doped polymer optical fibers," J. Opt. Soc. Am. B **16**(10), 1756–1767 (1999).
26. L. Bazzana, G. Lanzani, R. Xia, J. Morgado, S. Schrader, and D. G. Lidzey, "Plastic optical fibers with embedded organic semiconductors for signal amplification," in *Proceedings of the 16th international plastic optical fibers conference*, (Torino, Italy, 2007), 327–332.
27. M. Aslund, S. D. Jackson, J. Canning, A. Teixeira, and K. Lyytikainen-Digweed, "The influence of skew rays on angular losses in air-cladd fibres," Opt. Commun. **262**(1), 77–81 (2006).
28. G. E. Khalil, A. M. Adawi, A. M. Fox, A. Iraqi, and D. G. Lidzey, "Single molecule spectroscopy of red- and green-emitting fluorene-based copolymers," J. Chem. Phys. **130**(4), 044903 (2009).
29. C.-A. Bunge, R. Kruglov, and H. Poisel, "Rayleigh and Mie scattering in polymer optical fibers," J. Lightwave Technol. **24**(8), 3137–3146 (2006).
30. M. A. Illarramendi, "Side-illumination scattering theory in step-index polymer optical fibers," J. Opt. Soc. Am. B (to be published).
31. M. G. Kuzyk, *Polymer Fiber Optics: Materials, Physics, and Applications* (Taylor and Francis, 2007).
32. M. Abramowitz and I. A. Stegun, *Handbook of Mathematical Functions with Formulas, Graphs, and Mathematical Tables* (Dover Publications, 1965).

1. Introduction

Polymer optical fibers (POFs), also referred to as plastic optical fibers, are well-known in the optical-fiber field due to their robustness, large core diameters, high numerical apertures and low cost [1, 2]. Particularly, in the last few years POFs have been widely used both for short-haul communications links, where distances to cover are generally less than one kilometer [3], and for a wide variety of different sensing applications [4]. On the other hand, active doped POFs have also raised a great interest in the field of fiber lasers and amplifiers in the visible region [5–7] and even as active sensors [8–10]. The lower manufacturing temperatures of POFs as compared to glass fibers make it possible to embed a wide range of available materials into the fiber core. Specifically, amplifiers with high gain and efficient lasers have been obtained with organic dye-doped POFs [5, 11, 12]. Recently, conjugated polymers and related materials are being investigated as active dopants in plastic optical fibers (POFs) to provide amplification and switching capability [7, 13, 14]. Besides, doped fibers have been employed for fiber sensing applications. Moreover, the use of fluorescent POFs is the preferred option for environmental sensing or bio-sensing, either by measuring fluorescence intensity, fluorescence lifetime, or absorption coefficient [10].

In the aforementioned applications, namely, lasing, amplification or sensing, the overall system efficiency depends on the coupling of the incident light into the fiber and on the coupling of the generated emission to non-refracting directions in the fiber. Both couplings are usually described by means of the critical angle of the fiber ($(\theta_z)_c$), which can be expressed as a function of its numerical aperture (NA). In general, the value used for the NA in step-index multimode fibers is given by:

#159505 - $15.00 USD Received 5 Dec 2011; revised 23 Jan 2012; accepted 23 Jan 2012; published 9 Feb 2012

$$NA = \sqrt{n_{core}^{\ 2} - n_{clad}^{\ 2}}, \qquad (1)$$

where n_{core} and n_{clad} are, respectively, the refractive indices of their core and cladding. This expression, which some authors name meridional *NA* [15, 16], is related to the condition for incident rays into the fiber to be guided [17], since it indicates the maximum angle at which the fiber can accept the light that will be guided through it. This coupling of the incident light into the fiber affects strongly important parameters such as the threshold energy of fiber lasers [18]. On the other hand, the *NA* is also important to analyze the emission trapped in the fiber, because the internal critical angle indicates the fraction of light generated inside the fiber that is coupled into non-refracting directions [19]. For instance, this coupling determines the fraction β of the spontaneous emission that contributes to laser emission in fiber lasers or amplifiers [20] and it also affects the laser-threshold energy and the slope efficiency [21, 22]. Besides, in the analysis of the internal critical angle both guided rays and leaky (tunneling) rays have to be considered, since tunneling rays may not attenuate sufficiently to be neglected [17, 23]. This is because short doped fibers (of a few centimeters) are usually employed in fiber lasers and amplifiers.

In this work we perform a detailed study of the internal critical angle (maximum acceptance angle for the generated emission) in doped POFs. The fibers analyzed are POF samples of a few centimeters doped with a conjugated polymer. In particular, we analyze theoretically and experimentally the variation of the critical angle under different launching conditions when the fiber is pumped transversally to its axis. This type of excitation of the fiber, known as the side-illumination technique, was first proposed by Kruhlak and Kuzyk in 1999 and it is usually employed to characterize the emission and the optical losses in doped POFs [24, 25].The side-illumination method has recently been proposed for fluorescence sensing [9] because it has some advantages, such as higher signal-to-noise ratios than those offered by the usual sensor configurations based either on evanescent wave or guided light.

The paper is organized as follows. The experimental techniques are described in section 2. The theoretical model that describes the variation of the maximum acceptance angle as a function of launching conditions is explained in detail through section 3. The comparison between experimental and theoretical behaviors is shown and discussed in section 4. Finally, the summary of the work is presented in section 5.

2. Experimental set-up

Measurements have been performed in polymer optical fibers doped with the fluorene F8BT (poly(9,9-dioctylfluorene-co-benzothiadiazole)) at a concentration of 0.003%wt in the fiber core. The cladding material is not doped. The diameter of the fiber core is 980 μm and the thickness of the cladding is 20 μm. These doped fibers were produced using an adapted perform-drawing technique by the plastic fiber manufacturer Luceat S.p.A (Italy) and their fabrication details are described in [26]. Fiber samples were cut into 40 cm lengths, and the fiber ends were carefully polished by hand with polishing papers.

The far-field-pattern (FFP) intensity at the output of the fiber sample was measured as a function of the incident angle and of the launching lateral height when the fiber is illuminated transversally. Figure 1 shows the two geometrical configurations that have been analyzed. In the first one, the light is focused on the fiber axis with the incident plane containing the fiber axis, and the angle of incidence is varied (angular scan) (see Fig. 1(a)). In the second one, the direction of the incident light is fixed within an incident plane perpendicular to the fiber axis and, in this case, it is the position of the incident spot what actually varies (lateral scan) (see Fig. 1(b)).

The experimental set-up employed to measure the dependence of the FFP on the launching angle (α_i) and on the lateral height (y_P) can be seen in Fig. 2. A linearly polarized 375-nm-wavelength laser diode (8 mW) is used as light source. The laser beam is collimated and

#159505 - $15.00 USD Received 5 Dec 2011; revised 23 Jan 2012; accepted 23 Jan 2012; published 9 Feb 2012

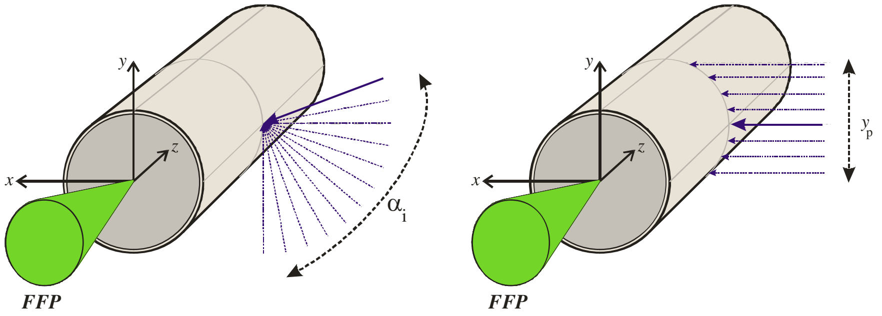

(a) (b)

Fig. 1. Measurement of the angular distribution of the emission at the output of the fiber as a function of the launching conditions. (a) Angular scan: a_i is the angle made by the incident beam with the normal to the fiber surface at $y_P = 0$ µm. The incident beam always lies in the *xz*-plane. (b) Lateral scan: y_P refers to the *y*-coordinate of the point of incidence relative to $y_P = 0$ µm. The incident beam lies in the *xy*-plane.

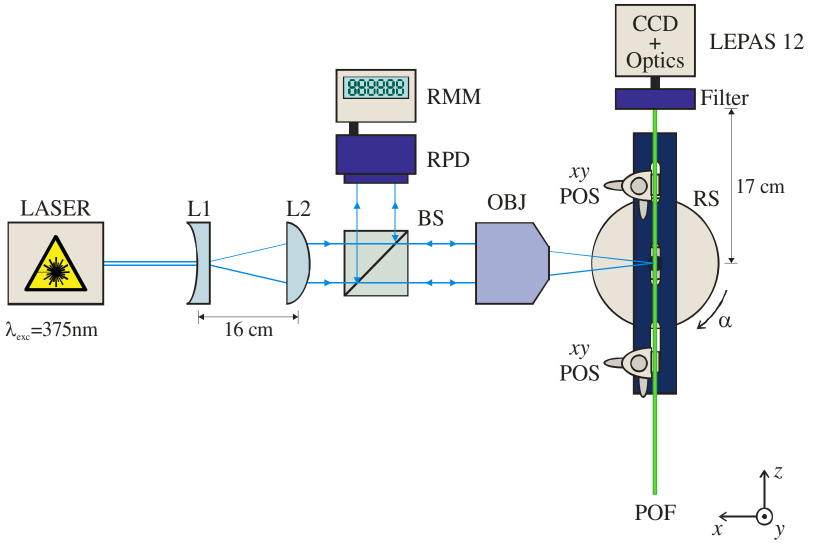

Fig. 2. Experimental set-up used to measure the angular distribution of the emission at the output end of doped POFs. Legend: L1 and L2: plane-concave and plane-convex lenses; BS: beam splitter; OBJ: 0.1-*NA* objective or cylindrical lens; *xy* POS: *xy*-micropositioner; RS: rotation stage; RPD: reference photodetector; RMM: reference multimeter; LEPAS-12: optical beam measurement system + integrated narrowband filter (emission wavelength: 535 nm). λ_{exc}: excitation wavelength.

expanded using lenses, L1 and L2, before impinging laterally on the active plastic optical fiber. By means of the beam splitter a reference signal is obtained to normalize the measurements. In order to keep both the divergence of the beam and the spot size as small as possible, a low-numerical-aperture objective (0.1-*NA*) focuses the incident beam on the fiber side. We have obtained a spot-size diameter at the focal plane below 10 µm. The doped POF sample is held by two *xy*-micropositioners standing on a rotation stage. The motion controller and the rotation stage are controlled by a computer, while the *xy*-micropositioners are adjusted manually. The automatized rotation stage, driven by a motion controller, allows us to change the launching angle in steps of 1 degree. In the case of the lateral scan, the step size is 25 µm. In both measurements (angular and lateral scans), the distance from the point of incidence to the output end of the fiber is 17 cm. The measurement of the far-field pattern (FFP) of the emission is obtained using the Hamamatsu LEPAS optical-beam-measurement system (exposure time of 5 ms). A narrow bandpass filter centered at the peak of the emission spectrum (535±2 nm) was placed at the entrance of the signal-measurement detector in order to perform the measurements at a single emission wavelength. From the analysis of the FFP images, we obtain the *NA* of the emission at the output of the fiber. This *NA* is related to the maximum acceptance angle as the sine of the half-angle at which the far-field angular intensity distribution has decreased to 5% of its maximum value [27]. Some photodegradation of the emission (photobleaching) is detected in our measurements. The value of the irradiance at the incident point of the fiber is in the range 1-2 kW/cm^2. The emission signal decreases in 15% from its initial value in the first two minutes, and, afterwards, the emission decreases more slowly (about 10% in the next 15 minutes from the minute 5). To reduce signal fluctuations in the measurements, these have been performed with a time step of 5 minutes between each image acquisition.

3. Theoretical modeling

In the side-illumination-fluorescence technique, the light source inside the fiber is the fluorescence generated when the fiber is illuminated from its lateral side. The emitted light intensity that reaches one of the fiber ends is detected and analyzed. The light detected is calculated as the emitted light within the maximum axial angle allowed for guided and tunneling rays. Although tunneling rays have larger losses than guided ones, they may not attenuate sufficiently in short distances to be neglected. Since the propagation distance through the analyzed fibers is extremely short (17 cm), we will assume that the propagation losses of both ray types (guided and leaky) are equal and negligible. Due to the geometry of excitation, it is assumed that the emission is generated by point sources placed along the refracted beam in the fiber core. A point source Q in our model has to be understood as an infinitesimal volume element (of length dx_Q) containing several atoms or molecules. Taking into account that the molecules of F8BT are distributed inhomogeneously in the polymer matrix [28], we can suppose that this infinitesimal volume emits isotropically, independently of the polarization of the refracted beam. The attenuation of the refracting beam due to the absorption will not be considered, because the absorption length at the incident wavelength is larger than the diameter of the fiber. The effects of the cladding thickness in our fibers have also been neglected and, consequently, we have taken the same value for the total fiber radius and the core radius (ρ_{core}). The doped fibers have been assumed to be step-index.

Let us start by analyzing the dependence of the FFP of the emitted light from the output fiber as a function of the angle of incidence (see Fig. 1(a) and Fig. 3(a)). In this case, the incident beam at the wavelength $\lambda = \lambda_{exc}$ is refracted at point $P(\rho_{core},0,z)$ of the fiber output surface and then it propagates across the core until it finally exits the fiber. Along its path through the core, the incident light is absorbed by a set of molecules at each point Q, which, in turn, emit light isotropically in all directions at wavelengths $\lambda = \lambda_{emi}$. Some of the emitted light will refract out of the fiber, and the remaining light lying within the internal critical angle $(\theta_z)_c$ will propagate through the fiber and it will be detected at one of the ends. Since the emission is generated from sources placed along the refracted beam, an analysis of the variation of $(\theta_z)_c$ inside the fiber is needed. By performing calculations similar to those exposed in [29, 30] the following expression for $\sin(\theta_z)_c$ corresponding to the beam emitting from the point source $Q(x_Q,0,z)$ is obtained:

$$\sin\left((\theta_z)_c\right)\left(x_Q,\phi_x\right) = \frac{\sqrt{1-n_{ratio}{}^2(\lambda_{emi})}}{\sqrt{1-\left(\dfrac{x_Q}{\rho_{core}}\sin\phi_x\right)^2}}, \tag{2}$$

where ϕ_x represents the angle of the emitted beam relative to the x-axis in the xy-plane and x_Q is the x-position of the source along the refracting beam (see Fig. 3(a)). The angle θ_z is

#159505 - $15.00 USD Received 5 Dec 2011; revised 23 Jan 2012; accepted 23 Jan 2012; published 9 Feb 2012

measured with respect to the fiber axis (z-axis). $n_{ratio}(\lambda_{emi})$ represents the quotient n_{clad}/n_{core} at $\lambda = \lambda_{emi}$. We see that the maximum acceptance angle of the fiber $(\theta_z)_c$ depends on x_Q and ϕ_x, and also on the refractive indices at $\lambda = \lambda_{emi}$, whereas it does not depend on the incident angle α_i. It can be seen that $\sin(\theta_z)_c$ expressed in Eq. (2) is higher than that corresponding to bound rays (meridional angle), which is a simplified expression of Eq. (2) for the case in which the fluorescence were produced from one source placed just at the center of the fiber ($x_Q = 0$), i.e.

$$\sin\left((\theta_z)_c\right) = \sqrt{1 - \left(\frac{n_{clad}}{n_{core}}\right)^2} = \sqrt{1 - n_{ratio}^{\;2}(\lambda_{emi})}. \tag{3}$$

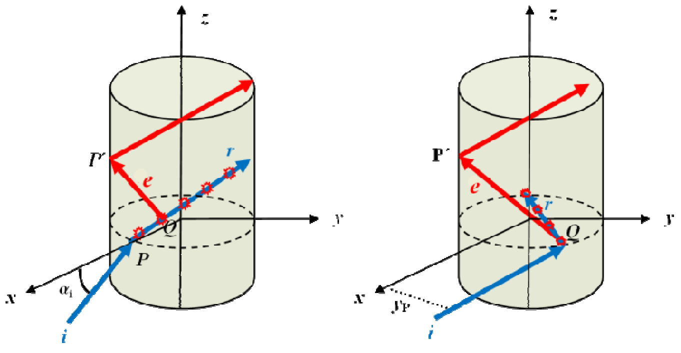

(a) (b)

Fig. 3. Geometrical arrangement of the POF with respect to the incident beam. (a) angular scan: α_i is the angle made by the incident beam with the normal to the fiber surface at $y_P = 0$ µm. The incident beam ***i*** always lies in the xz-plane. ***e*** represents the emitted beam, while ***r*** is the refracted beam. (b) lateral scan: y_P refers to the y-coordinate of the point of incidence relative to $y_P = 0$ µm. The incident beam ***i*** lies in the xy-plane. ***e*** represents the emitted beam, while ***r*** is the refracted beam.

A model assuming that all the fluorescence is produced at one point in the center of the fiber, together with Eq. (3), has been used to analyze the emission intensity of a doped fiber as a function of propagation distance [24, 31]. The fact that the critical angle calculated for any emitted beam (Eq. (2) is higher than that obtained from Eq. (3) indicates that both guided and leaky (tunneling) rays are excited inside the fiber as the refracted ray propagates along the fiber [23].

Since $(\theta_z)_c$ cannot exceed $\pi/2$ ($\sin(\theta_z)_c \leq 1$), it is required that x_Q and ϕ_x satisfy the following constraint:

$$1 > n_{ratio}^{\;2}(\lambda_{emi}) \geq \left(\frac{x_Q}{\rho_{core}} \sin\phi_x\right)^2. \tag{4}$$

This condition defines a valid region in terms of the source position (x_Q) and the emitted direction (ϕ_x) where guided and tunneling rays are generated within the fiber. As an example, Fig. 4 shows the representation of $\sin(\theta_z)_c$ as a function of both x_Q and ϕ_x corresponding to the doped plastic optical fiber analyzed. This representation has been obtained with the characteristic fiber parameters supplied by the manufacturer ($n_{core}(\lambda_{emi}) = 1.495$, $r_{core} = 490$ µm *and* $NA_{meriodional} = (n_{core}^{\;2} - n_{clad}^{\;2})^{1/2} = 0.5$). It can be seen that the curves are symmetrical respect to $x_Q = 0$ and $\phi_x = \pi$ and that there are some source points (near to the fiber interfaces) emitting light in certain specific directions whose maximum acceptance angle is not defined. Those emitted beams generated very close to the core-cladding interface that yield imaginary values for $\sin(\theta_z)_c$ can be interpreted as evanescent modes along the fiber axis. These modes describe the energy stored in the immediate vicinity of fiber discontinuities [17]. As the

#159505 - $15.00 USD Received 5 Dec 2011; revised 23 Jan 2012; accepted 23 Jan 2012; published 9 Feb 2012

quotient $n_{ratio}(\lambda_{emi})$ approaches the value 1, the forbidden regions, where $(\theta_z)_c$ is not defined, become smaller and, consequently, the effects of the truncation of the sine function on the emitted intensity are insignificant. The imposition that $(\theta_z)_c$ cannot exceed $\pi/2$ and its effects on the near-field patterns and on the scattered light curves of step-index fibers have been reported in [23].

By considering the restrictions for $\sin(\theta_z)_c$ (Eq. (4)), we can now calculate an average of the sine of $(\theta_z)_c$ for the doped fiber as follows:

$$\begin{aligned}
&\left\langle \sin\left((\theta_z)_c\right)\right\rangle = \\
&\left[\int_0^{\arcsin(n_{ratio})} d\phi_x \int_{-\rho_{core}}^{+\rho_{core}} \sin(\theta_z)_c(x_Q,\phi_x)dx_Q + \int_{\pi-\arcsin(n_{ratio})}^{\pi} d\phi_x \int_{-\rho_{core}}^{+\rho_{core}} \sin(\theta_z)_c(x_Q,\phi_x)dx_Q \; + \right. \\
&\left. + \int_{\arcsin(n_{ratio})}^{\pi-\arcsin(n_{ratio})} d\phi_x \int_0^{\frac{\rho_{core} n_{ratio}}{\sin\phi_x}} \sin(\theta_z)_c(x_Q,\phi_x)dx_Q \right] \Bigg/ \left[\int_0^{\arcsin(n_{ratio})} d\phi_x \int_{-\rho_{core}}^{+\rho_{core}} dx_Q \; + \right. \\
&\left. + \int_{\pi-\arcsin(n_{ratio})}^{\pi} d\phi_x \int_{-\rho_{core}}^{+\rho_{core}} dx_Q + \int_{\arcsin(n_{ratio})}^{\pi-\arcsin(n_{ratio})} d\phi_x \int_0^{\frac{\rho_{core} n_{ratio}}{\sin\phi_x}} dx_Q \right].
\end{aligned} \tag{5}$$

This expression has been worked out and the result obtained is the following:

$$\begin{aligned}
&\left\langle \sin\left(\theta_z\right)_c \right\rangle = \\
&= \frac{i\sqrt{1-n_{ratio}{}^2(\lambda_{emi})}}{2\left(\arcsin\left(n_{ratio}(\lambda_{emi})\right) + n_{ratio}(\lambda_{emi})\log\left(\cot\left(\frac{\arcsin\left(n_{ratio}(\lambda_{emi})\right)}{2}\right)\right)\right)} \\
&\sum_{k=1}^{\infty}\left(\frac{\left(-in_{ratio}(\lambda_{emi})-\sqrt{1-n_{ratio}{}^2(\lambda_{emi})}\right)^k}{k^2} - \frac{\left(in_{ratio}(\lambda_{emi})-\sqrt{1-n_{ratio}{}^2(\lambda_{emi})}\right)^k}{k^2}\right. \\
&\left. + \frac{\left(-in_{ratio}(\lambda_{emi})+\sqrt{1-n_{ratio}{}^2(\lambda_{emi})}\right)^k}{k^2} - \frac{\left(in_{ratio}(\lambda_{emi})+\sqrt{1-n_{ratio}{}^2(\lambda_{emi})}\right)^k}{k^2}\right).
\end{aligned} \tag{6}$$

An approximated average of the sine of $(\theta_z)_c$ can be calculated by taking all the point sources placed in a reduced region, $-\rho_{core}\, n_{ratio}(\lambda_{emi}) \le x_Q \le \rho_{core}\, n_{ratio}(\lambda_{emi})$ and $0 \le \phi_x \le 2\pi$, i.e.

$$\left\langle \sin(\theta_z)_c \right\rangle = \frac{\int_{-n\rho_{core}}^{+n\rho_{core}} dx_Q \int_0^{2\pi} \sin(\theta_z)_c\left(x,\phi_x\right)d\phi_x}{\int_{-n\rho_{core}}^{+n\rho_{core}} dx_Q \int_0^{2\pi} d\phi_x}. \tag{7}$$

This selected integration region can be seen in Fig. 4. The analytical expression corresponding to Eq. (7) can be written as:

$$\left\langle \sin\left(\theta_z\right)_c \right\rangle = \sqrt{1-n_{ratio}{}^2(\lambda_{emi})}\; {}_3F_2\,[\{\tfrac{1}{2},\tfrac{1}{2},\tfrac{1}{2}\},\{1,\tfrac{3}{2}\},n_{ratio}{}^2(\lambda_{emi})], \tag{8}$$

where ${}_3F_2\left[\{1/2,1/2,1/2\},\{1,3/2\},n_{ratio}{}^2(\lambda_{emi})\right]$ represents the generalized hypergeometric function [32]. The average of $\sin(\theta_z)_c$ obtained under this assumption (Eq. (8)) does not differ very much from the one calculated exactly (Eq. (6)) [30], since it represents the average of the sine of the critical angle when the contribution of some tunneling rays is neglected,

#159505 - $15.00 USD Received 5 Dec 2011; revised 23 Jan 2012; accepted 23 Jan 2012; published 9 Feb 2012

particularly those with a high $(\theta_z)_c$. Notice that Eq. (6) and Eq. (8) depend only on $n_{ratio}(\lambda_{emi})$. By averaging Eq. (2) in the reduced region and by taking into account that the emission is isotropic, we have obtained the dependence of the sine of $(\theta_z)_c$ with the position of the emission source. The average of the sine is calculated as follows:

$$\left\langle \sin(\theta_z)_c \right\rangle \left(x_Q \right) = \frac{\int_0^{2\pi} \sin(\theta_z)_c \left(x_Q, \phi_x \right) d\phi_x}{\int_0^{2\pi} d\phi_x}. \tag{9}$$

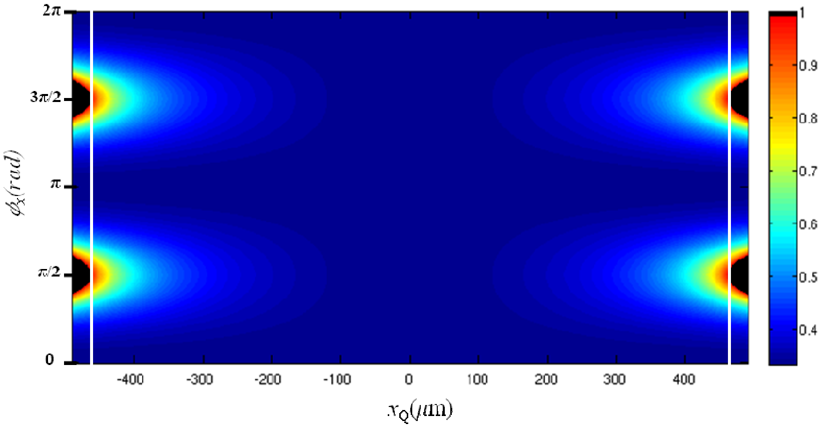

Fig. 4. 2D image of the $\sin(\theta_z)_c$ as a function of parameters x_Q and ϕ_x for angular incidence. Black painted areas indicate the forbidden regions for x_Q and ϕ_x giving no real $\sin(\theta_z)_c$. White solid lines correspond to $x_Q = \pm \rho_{core} n_{ratio}(\lambda_{emi})$. Calculations performed with $NA_{meridional} = 0.5$, $n_{core}(\lambda_{emi}) = 1.495$, and $\rho_{core} = 490$ µm.

The analytical expression obtained for this calculation (Eq. (9)) can be expressed as:

$$\left\langle \sin\left(\theta_z\right)_c \right\rangle \left(x_Q \right) = \frac{\sqrt{1 - n_{ratio}^{\ 2}(\lambda_{emi})}}{\pi} \left(K\left(\frac{x_Q}{\rho_{core}} \right)^2 + \frac{K\left(\dfrac{\left(x_Q / \rho_{core} \right)^2}{\left(x_Q / \rho_{core} \right)^2 - 1} \right)}{\sqrt{1 - \left(x_Q / \rho_{core} \right)^2}} \right), \tag{10}$$

where K is the complete elliptic integral of the first kind [32]. The dependence of $\sin(\theta_z)_c$ on the position of the emission point source x_Q along the path of the refracting beam in the fiber core has been plotted in Fig. 5. In the same figure we have included the averages of the sine of $(\theta_z)_c$ obtained from Eq. (6) and approximately estimated from Eq. (8) as well as the value of $\sin(\theta_z)_c$ for bound rays (see Eq. (3)). The symmetrical curve obtained indicates that the closer to the core-cladding interface the point source is placed, the larger its maximum acceptance angle is. It can be observed that $\sin(\theta_z)_c$ increases from the value corresponding to bound rays (i.e. $\sin(\theta_z)_c$ for one point source placed at the center of the fiber) to $<\sin(\theta_z)_c>$ obtained from Eq. (6). The relative difference between $\sin(\theta_z)_c$ obtained from Eq. (3) and from Eq. (6) is around 12%, whereas the relative difference between the values obtained from Eqs. (6) and (8) is only 1.5% (much smaller, as expected).

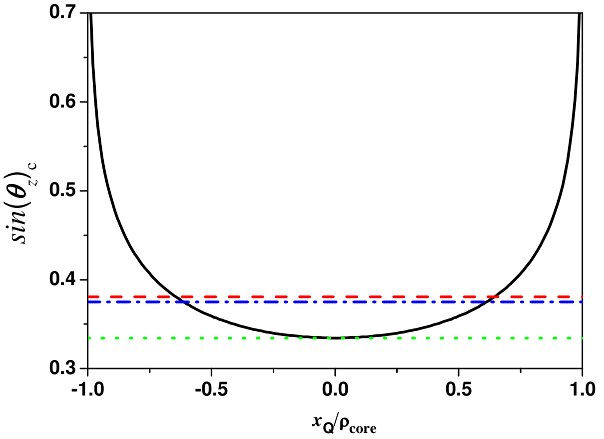

Fig. 5. Average value of the sine of the critical angle as a function of the position of the emission point source in the fiber core, or $<\sin(\theta_z)_c>(x_Q)$, calculated from Eq. (10) (solid line); meridional $\sin(\theta_z)_c = 0.335$, from Eq. (3) (dotted line); $<\sin(\theta_z)_c> = 0.375$ obtained from Eq. (8) (dash-dotted line); $<\sin(\theta_z)_c> = 0.381$ obtained from Eq. (6) (dashed line). Calculations performed with $NA_{meridional} = 0.5$, $n_{core}(\lambda_{emi}) = 1.495$, and $r_{core} = 490$ μm.

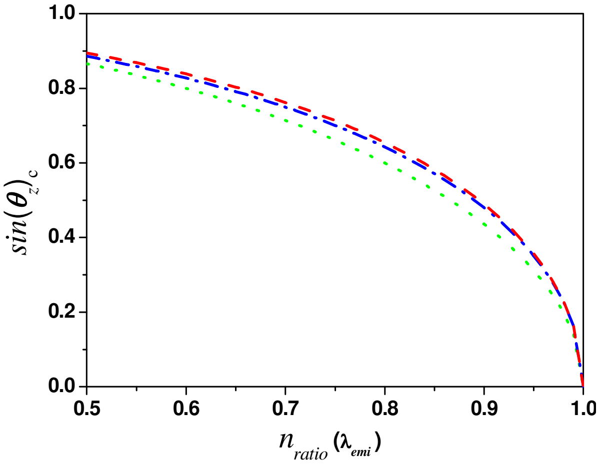

Fig. 6. Sine of the critical angle as a function of nratio(λ_{emi}). Meridional $\sin(\theta_z)_c$ obtained from Eq. (3) (dotted line); $<\sin(\theta_z)_c>$ from Eq. (8) (dotted line); $<\sin(\theta_z)_c>$ from Eq. (6) (dash-dotted line).

In Fig. 6 we have compared the variation with $n_{ratio}(\lambda_{emi})$ of the values for $\sin(\theta_z)_c$ obtained from Eq. (6), Eq. (8) and Eq. (3). The values obtained from Eq. (6) and those calculated in the reduced region (Eq. (8)) differ in less than 2% at any value of $n_{ratio}(\lambda_{emi})$. On the other hand, the difference between the sine of the maximum acceptance angle obtained from Eq. (3) and that from Eq. (6) increases with $n_{ratio}(\lambda_{emi})$, particularly from 3% to 17%. It can be verified that, if $n_{ratio}(\lambda_{emi})$ tends to 1, the values of the average $\sin(\theta_z)_c$ obtained from Eqs. (6) and (8) are equal, and that the quotient between this average value and that obtained from Eq. (3) can be expressed as:

$$\frac{\left\langle \sin(\theta_z)_c \right\rangle}{\sqrt{1-n_{ratio}{}^2(\lambda_{emi})}} = \frac{4Catalan}{\pi}, \tag{11}$$

#159505 - $15.00 USD Received 5 Dec 2011; revised 23 Jan 2012; accepted 23 Jan 2012; published 9 Feb 2012

where Catalan constant has a numerical value ≅ 0.915966. This expression gives the maximum difference between the average value and the meridional one (17%).

Now let us analyze the variation of $\sin(\theta_z)_c$ with the lateral height of the incident beam. The geometrical situation corresponding to this excitation was plotted in Figs. 1(b) and 3(b). The calculation of the sine of $(\theta_z)_c$ for any point source located at the refracting beam (at point Q) in the xy-plane gives the following expression [29, 30]:

$$\sin(\theta_z)_c\left(x_Q{}',\phi_x,y_P\right)=\frac{\sqrt{1-n_{ratio}{}^2(\lambda_{emi})}}{\sin\Delta}, \tag{12}$$

with

$$\sin\Delta=\left[1-\frac{\left(x'_Q\right)^2+\left(\dfrac{y_P}{n_{core}(\lambda_{ext})}\right)^2}{\rho_{core}^2}\cdot\sin^2\left(\phi_x+\arctan\left(\frac{y_P}{n_{core}(\lambda_{ext})x'_Q}\right)+\arctan\left(\frac{y_P}{\sqrt{\rho_{core}^2-y_P^2}}\right)-\arcsin\left(\frac{y_P}{\rho_{core}n_{core}(\lambda_{ext})}\right)\right)\right]^{\frac{1}{2}}.$$

This expression depends now on three variables: x'_Q, or position of the source along the refracting beam (the x'-axis is directed along the path covered by the refracted beam); ϕ_x, or angle of the emitted beam relative to the x-axis in the xy-plane; and $y_{P,}$ or height of the incident point on the fiber. In contrast to the expression of $\sin(\theta_z)_c$ obtained for the angular dependence, $\sin(\theta_z)_c$ depends now on the refractive index of the fiber core at the excitation wavelength, in addition to the refractive indices of the core and the cladding at the emission wavelength.

As commented before, a constraint for the allowed values of the source position (x'_Q), the direction of the emitted beam (ϕ_x) and the lateral height (y_P) is found in order to obtain real-valued arguments for the sine function in Eq. (12). This restriction defines a valid region where bound and tunneling rays are created within the fiber. It can be expressed as:

$$1 > n_{ratio}{}^2(\lambda_{emi}) \geq \frac{\left(x'_Q\right)^2+\left(\dfrac{y_P}{n_{core}(\lambda_{ext})}\right)^2}{\rho_{core}^2}\cdot\sin^2\left(\phi_x+\arctan\left(\frac{y_P}{n_{core}(\lambda_{ext})x'_Q}\right)+\arctan\left(\frac{y_P}{\sqrt{\rho_{core}^2-y_P^2}}\right)-\arcsin\left(\frac{y_P}{\rho_{core}n_{core}(\lambda_{ext})}\right)\right). \tag{13}$$

The modes associated to the regions that yield imaginary values for $\sin(\theta_z)_c$ can be interpreted as non-propagating modes whose energy is stored close to fiber discontinuities. As an example, Fig. 7 shows the representation of $\sin(\theta_z)_c$ (ϕ_x,x'_Q) as a function of ϕ_x and x'_Q for a lateral height $y_P = \rho_{core}/2$, in which there are some forbidden regions corresponding to specific values of ϕ_x and x'_Q whose maximum acceptance angle is not defined. The results correspond to a doped POF fiber with $NA_{meriodional} = 0.5$, $n_{core}(\lambda_{emi}) = 1.495$, and $\rho_{core} = 490$ μm. The refractive index of the fiber core at λ_{exc} has been taken to be the same as that at λ_{emi}. In contrast to Fig. 4, the curves are not symmetrical with respect to $x'_Q = 0$ and to $\phi_x = \pi$. Notice that if variable y_P were 0, Eqs. (12) and (13) would be simplified to Eqs. (2) and (4), respectively.

By taking into account all the previous considerations, the average of the sine of the critical angle at an incidence y_P can be calculated over the region R where Eq. (13) is satisfied, i.e.

#159505 - $15.00 USD Received 5 Dec 2011; revised 23 Jan 2012; accepted 23 Jan 2012; published 9 Feb 2012

$$\left\langle \sin(\theta_z)_c \right\rangle \left(y_P \right) = \frac{\int_R \int_R \sin(\theta_z)_c \left(x'_Q, \phi_x, y_P \right) dx'_Q \, d\phi_x}{\int_R \int_R dx'_Q \, d\phi_x}. \tag{14}$$

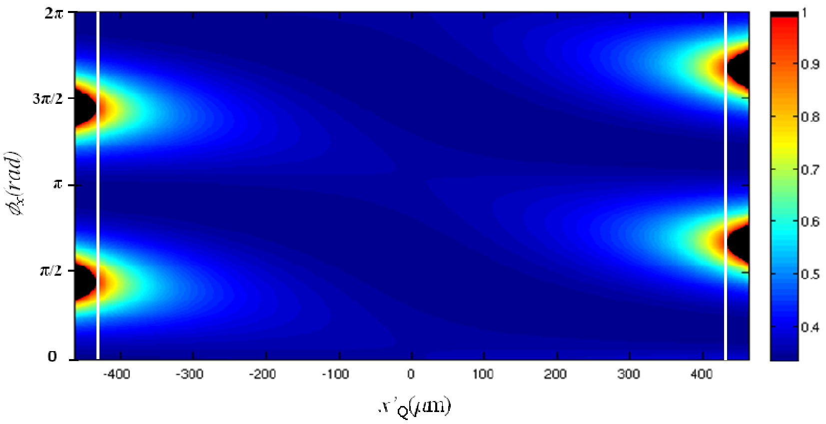

Fig. 7. 2D image of $\sin(\theta_z)_c$ as a function of parameters x'_Q and ϕ_x for lateral incidence. The lateral height y_P has been fixed to $y_P = \rho_{core}/2$. Black areas indicate the forbidden regions for x'_Q and ϕ_x giving no real $\sin(\theta_z)_c$. The white solid vertical lines correspond to x'_Q(min) and x'_Q(max). Calculations performed with $NA_{meridional} = 0.5$, $n_{core}(\lambda_{emi}) = n_{core}(\lambda_{exc}) = 1.495$, and $\rho_{core} = 490$ µm.

If we choose the limited region, $0 \le f_x \le 2\pi$, and $x'_Q(\text{min}) \le x'_Q \le x'_Q(\text{max})$, where *x'*$_Q$*(min)* and *x'*$_Q$*(max)* are defined as

$$x'_Q(\text{min}) = -\sqrt{\rho_{core} n_{ratio}{}^2(\lambda_{emi}) - \frac{y_P{}^2}{n_{core}{}^2(\lambda_{ext})}} \qquad x'_Q(\text{max}) = +\sqrt{\rho_{core} n_{ratio}{}^2(\lambda_{emi}) - \frac{y_P{}^2}{n_{core}{}^2(\lambda_{ext})}}, \tag{15}$$

the average of the sine of the critical angle at an incidence y_P can be calculated as follows:

$$\left\langle \sin(\theta_z)_c \right\rangle \left(y_P \right) = \frac{\int_{x'_Q(\text{min})}^{x'_Q(\text{max})} dx'_Q \int_0^{2\pi} \sin(\theta_z)_c \left(x'_Q, \phi_x, y_P \right) d\phi_x}{\int_{x'_Q(\text{min})}^{x'_Q(\text{max})} dx'_Q \int_0^{2\pi} d\phi_x}. \tag{16}$$

This approach represents the average $\sin(\theta_z)_c$ for the emitted light in the fiber by neglecting the contribution of some tunneling rays. As we have shown before, the differences between the $<\sin(\theta_z)_c>$ from the exact Eq. (14) and the approximated Eq. (16) are expected to be small [30].

The theoretical variation of $\sin(\theta_z)_c$ with the incidence position y_P for the fiber analyzed can be observed in Fig. 8. The obtained symmetrical curves indicate that the closer the incidence point is to the core-cladding interface, the larger the maximum acceptance angle is. By integrating the previous equation with respect to y_P we obtain the average value of the sine of the critical angle for all the possible lateral incidences y_P, from $-\rho_{core}$ to $+\rho_{core}$. This value of $<\sin(\theta_z)_c>$ would correspond to the situation where all the section of the fiber is illuminated laterally, for instance by using a cylindrical lens. The obtained average values have been included in Fig. 8 together with the sine of the maximum acceptance angle for bound rays (Eq. (3)). The values for $<\sin(\theta_z)_c>$ obtained from the exact average of $\sin(\theta_z)_c$ (Eq. (14)) and from Eq. (16) differ from the value obtained from Eq. (3) in around 12% and 11%, respectively, for the analyzed fiber.

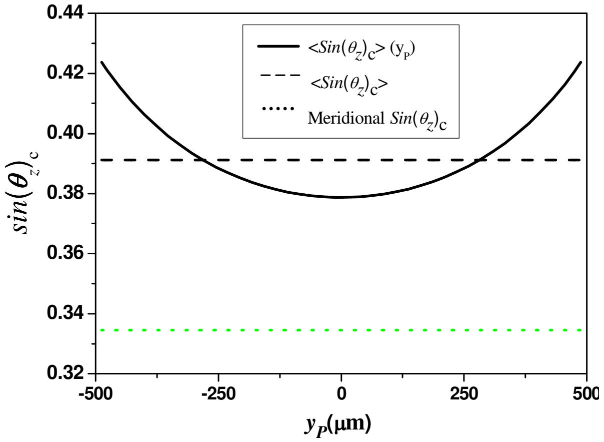

Fig. 8. Average of the sine of the critical angle as a function of y_P, i.e. $<\sin(\theta_z)_c>(y_P)$, calculated from Eq. (14) (solid line); meridional $\sin(\theta_z)_c = 0.335$ from Eq. (3) (dotted line); $<\sin(\theta_z)_c> = 0.391$ (for all values of y_P) (dashed line). Calculations performed with $NA_{meridional} = 0.5$, $n_{core}(\lambda_{emi}) = n_{core}(\lambda_{exc}) = 1.495$, and $r_{core} = 490$ µm.

4. Results and discussion

In this section we compare the results obtained from the theoretical model with the experimental ones. In Fig. 9 we can observe 2D images of the angular distribution of the emission at the output end of the fiber for three different incident angles of the launching beam, namely, $\alpha_i = -45°$, $\alpha_i = 0°$ and $\alpha_i = +45°$.

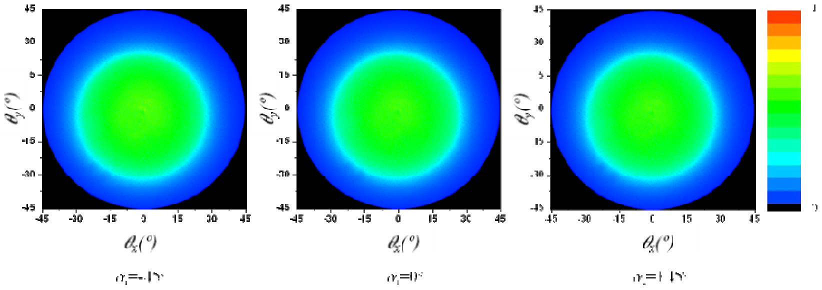

Fig. 9. Normalized FFP of the emission ($\lambda_{emi} = 535$ nm) at the output of the fiber for different angles of incidence: $\alpha_i = -45°$, $\alpha_i = 0°$, and $\alpha_i = +45°$.

From the data matrix recorded, precise measured values for the *NA* have been calculated and plotted in Fig. 10. In agreement with the theoretical model, we can observe that *NA* hardly varies with the angle of incidence of the exciting beam. In the same figure we can observe the fitting of the experimental *NA* to the equation $NA = <\sin(\theta_z)_c> n_{core}(\lambda_{emi})$ where $<\sin(\theta_z)_c>$ is given by Eq. (6). As can be seen, the agreement obtained is very good. From the fitting, the following values of the parameters have been obtained: $NA_{meridional} = 0.49$ and $n_{core}(\lambda_{emi}) = 1.495$. These are almost identical to the characteristic parameters of the fiber used in the previous section.

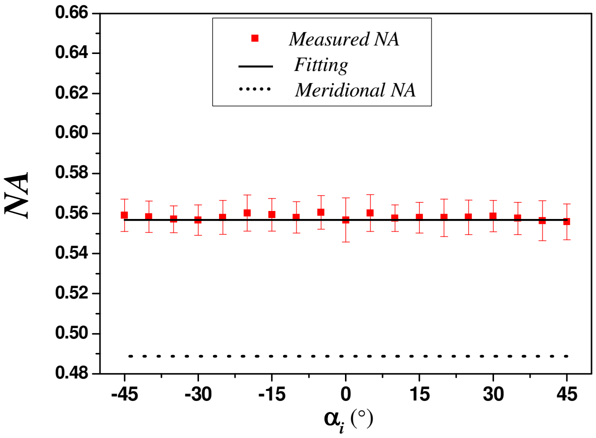

Fig. 10. Evolution of *NA* at the output end of an F8BT-doped POF sample as a function of the angle of incidence: experimental values (■) and *NA* = 0.557 calculated from the fitting to Eq. (6) (solid line). $NA_{meridional}$ = 0.489 calculated from Eq. (3) (dotted line).

Concerning the results for the lateral scan, in Fig. 11 we show 2D images of the measured FFP of the emission at 535 nm for three different positions of the exciting beam, namely, y_P = –450 µm, y_P = 0 µm and y_P = +450 µm.

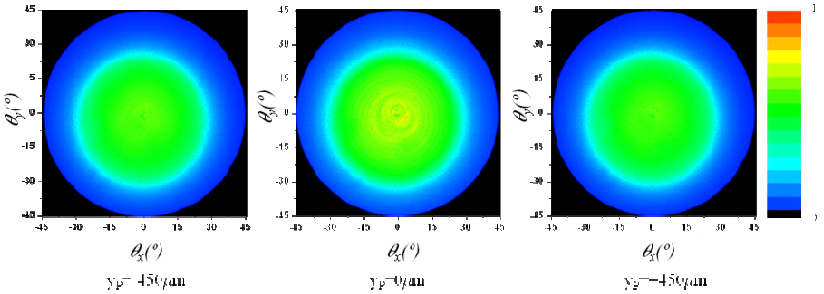

Fig. 11. Normalized FFP of the emission (λ_{emi} = 535 nm) at the output of the fiber for different positions of the lateral exciting beam: y_P = –450 µm, y_P = 0 µm, and y_P = +450 µm.

The experimental *NA* of the emission at the output of the fiber as a function of y_P is shown in Fig. 12. As expected from theoretical predictions, we detect a noticeable increase in the *NA* as the incidence beam moves up and down towards the upper and lower edges of the fiber, with a minimum value when the fiber is excited at $y_P = 0$ (*NA* = 0.557). The fitting of the experimental values to the equation $NA = \langle\sin(\theta_z)_c\rangle(y_P)\, n_{core}(\lambda_{emi})$, where $\langle\sin(\theta_z)_c\rangle(y_P)$ is given by Eq. (14), has also been included in Fig. 12. The fiber parameters obtained from this fitting are the same as those obtained in the fitting of Fig. 10 ($NA_{meridional}$ = 0.49 and $n_{core}(\lambda_{emi}) = n_{core}(\lambda_{exc})$ = 1.495). As can be observed, both curves are in fairly good agreement again. Finally, the experimental value for *NA* obtained by exciting all the lateral surface of the fiber with a cylindrical lens has been included in the figure as a dashed line and it has been compared with the theoretical calculation of the average $\sin(\theta_z)_c$ for all the possible lateral incidences y_P, from $-\rho_{core}$ to $+\rho_{core}$ (dash-dotted line). It can be observed that the measured value is very close to the theoretically predicted average $\langle\sin(\theta_z)_c\rangle$ (0.575 and 0.572, respectively). On the other hand, we can also notice that the meridional *NA* (0.49) is 15% lower than the averaged *NA*.

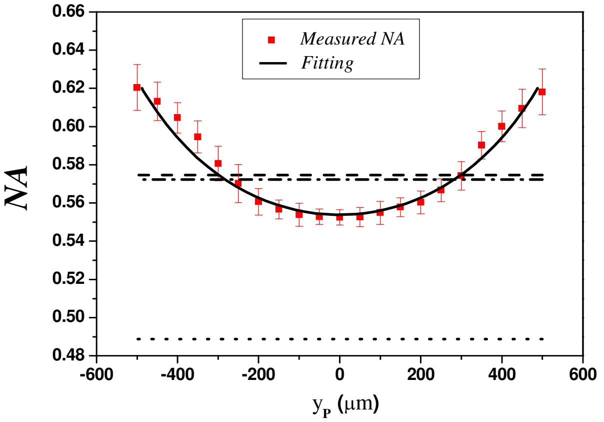

Fig. 12. Evolution of the *NA* at the output end of the F8BT-doped POF as a function of y_P: Experimental values (■); fitting to $NA = \langle \sin(\theta_z)_c \rangle (y_P)\, n_{core}(\lambda_{emi})$ (solid line); $NA_{meridional} = 0.489$ obtained from Eq. (3) (dotted line); theoretical average $NA = \langle \sin(\theta_z)_c \rangle\, n_{core}(\lambda_{emi}) = 0.572$ (dash-dotted line); measured *NA* exciting the fiber with a cylindrical lens $NA = 0.575$ (dashed line).

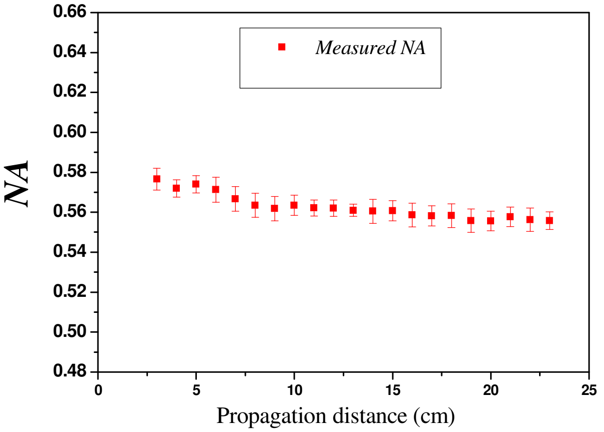

Fig. 13. Evolution of the measured *NA* of the emission (λ_{emi} = 535 nm) for the F8BT-doped POF as a function of the propagation distance.

The use of the more accurate greater *NA*, in comparison with the usually employed meridional one, gives rise to differences in the calculated values of some important parameters related to the performance of active fibers. For instance, a parameter closely related to *NA* is the fraction β of the spontaneous emission that contributes to laser emission. As shown in [21], this has a quadratic dependence on *NA* for step-index fibers, so the use of the corrected value would give a result for β that is 30% higher than the one calculated using $NA_{meridional}$. On the other hand, although the difference arising in the threshold when we use $NA_{meridional}$ instead of the corrected one is not significant (at least in step-index doped POFs), the change is much more important in the case of the slope efficiency. Specifically, we have obtained, from computational simulations similar to those reported in [21], that the threshold in F8BT-doped fibers hardly varies when $NA_{meridional}$ is changed to the corrected *NA*. However, we have obtained, for the same doped fiber, that the slope efficiency (η) varies much more rapidly with *NA*, in a way proportional to NA^2, i.e., $\eta = c_1 NA^2$, where c_1 is a constant. Therefore, since the relative difference between both values of *NA* is about 15%, the relative increase in the efficiency would be of 30%.

Finally, in Fig. 13 we illustrate the evolution with the propagation distance through the doped fiber of the *NA* measured at the end of the fiber. We can observe that there is a low decrease in the angular distribution of the emission along the doped POF sample. Specifically, the measured *NA* decreases from 0.571 to 0.558 (2%) in 17 centimeters, which is the propagation distance used in our measurements. This very slight reduction in the value of *NA* with propagation distance validates the assumption made in the theoretical model, in which propagation losses in the calculation of the critical angle are neglected.

5. Conclusions

For the first time, the critical angle for the emission generated in doped POFs has been theoretically and experimentally analyzed by using the side-illumination fluorescence technique. The experimental study has been performed in an F8BT-doped polymer optical fiber. A good agreement between the theoretical and the experimental results has been obtained both qualitatively and quantitatively. It is shown that, in all cases, the critical angles are noticeably higher than the meridional one corresponding to a single source placed at the fiber axis. In the case that all the lateral surface of the fiber is illuminated, the difference between the measured *NA* and the meridional approximation can be up to 15%. This change would affect the value of important parameters related to the performance of doped fibers. Specifically, the corrected value of the output efficiency in the considered doped fiber would be 30% higher than the one calculated using the meridional approximation.

Acknowledgments

This work was supported by the institutions Ministerio de Ciencia e Innovación, Gobierno Vasco/Eusko Jaurlaritza, and Diputación Foral de Bizkaia/Bizkaiko Foru Aldundia, under projects TEC2009-14718-C03-01, GIC07/156-IT-343-07, UFI11/16 (UPV-EHU), AISHA + , AIRHEM-II, S-PR10UN04, S-PE09CA03 and DENSHIA, and 06-12-TK-2010-0022, respectively.